Dynamic Modeling and Control System Definition for a Micro-CSP Plant Coupled With Thermal Storage Unit

Proceedings of ASME Turbo Expo 2014: Turbine Technical Conference and Exposition
GT2014
June 16 – 20, 2014, Düsseldorf, Germany

GT2014-27132

DYNAMIC MODELING AND CONTROL SYSTEM DEFINITION FOR A MICRO-CSP PLANT COUPLED WITH THERMAL STORAGE UNIT

Melissa K. Ireland[a*], **Matthew S. Orosz**[b], **J.G. Brisson**[b]
[a] GE Aviation
Lynn, Massachusetts 01910
[a,b] Massachusetts Institute of Technology
Cambridge, Massachusetts 02139
Email: mki4@mit.edu

Adriano Desideri, Sylvain Quoilin
Thermodynamics Laboratory
University of Liège
B-4000 Liège, Belgium

ABSTRACT

Organic Rankine cycle (ORC) systems are gaining ground as a means of effectively providing sustainable energy. Coupling small-scale ORCs powered by scroll expander-generators with solar thermal collectors and storage can provide combined heat and power to underserved rural communities. Simulation of such systems is instrumental in optimizing their control strategy. However, most models developed so far operate at steady-state or focus either on ORC or on storage dynamics. In this work, a model for the dynamics of the solar ORC system is developed to evaluate the impact of variable heat sources and sinks, thermal storage, and the variable loads associated with distributed generation. This model is then used to assess control schemes that adjust operating conditions for daily environmental variation.

NOMENCLATURE

A	Area, m^2.
D_o	Outer diameter, m.
f	Friction factor.
h	Enthalpy, Jkg^{-1}.
HL	Heat loss, Wm^{-1}.
IAM	Incidence angle modifier.
I_b	Beam radiation, Wm^{-2}.
k_{ins}	Insulation thermal conductivity, $W(mK)^{-1}$.
L_{col}	Total collector length, m.
$\dot{m}$	Mass flow rate, kgs^{-1}.
M_w	Mass of metal wall between fluids, kg.
N_{rot}	Rotational speed, s^{-1}.
p	Pressure, Pa.
$\dot{Q}$	Heat flow, W.
v_w	Wind velocity, ms^{-1}.
V	Volume, m^3.
$\dot{V}_s$	Ideal volume flow rate, m^3s^{-1}.
t_{ins}	Insulation thickness, m.
T	Temperature, °C.
W_{col}	Collector width, m.
$\dot{W}$	Power, W.
η	Efficiency.
ν	Specific volume, m^3kg^{-1}.
ϕ	Expander filling factor.
θ	Incidence angle, °.

Subscripts

amb	Ambient.
cross	Cross-sectional.
el	Electrical.
em	Electromechanical.
ev	Evaporator.
ex	Exhaust.
exp	Expander.
nom	Nominal.
p	Pump.
su	Supply.
s	Swept, isentropic, or surface.

*Address all correspondence to this author.

INTRODUCTION

Micro-CSP (concentrating solar power) plants based on ORCs present a cost-effective solution to the challenge of supplying heating, cooling, and electricity for rural health and education centers outside the range of a centralized grid [1]. Although ORCs tend to have lower efficiencies than traditional steam Rankine cycles, the thermodynamic properties of organic fluids lead to several distinct advantages in the low to medium power range. For example, the slope of the vapor saturation curve and the super-atmospheric saturation pressures of some organic fluids preclude the need for superheating and the removal of non-condensable gases, respectively, used in steam Rankine cycles, reducing the complexity, cost, and maintenance requirements [2].

Coupling micro-CSP plants with thermal storage allows for an increase in daily operating time and also for a damping of the rapid variations that may be seen in the solar input (e.g., due to clouds). However, input temperatures during normal operation may still vary as much as $\pm 20^{\circ}$C throughout the year. Furthermore, using readily-available components, like re-purposed HVAC (heating, ventilation, and air conditioning) scroll compressors for expansion, while cost-effective, results in the additional design objective of preventing over- or under-expansion of the working fluid in the fixed-volume ratio scroll machines. The effective design of such a system depends on modeling and identifying a control strategy with the ability to adjust to transient operating conditions.

Several authors have simulated solar thermal ORC systems in steady-state. Orosz [1] created a physical and economic model in EES (Engineering Equation Solver) that predicted solar ORC performance over a year for the specified location and system components. This model condensed the hourly irradiance variation over the year into a single average value reduced by expected cloud cover to predict net power output and daily and annual energy production. McMahan [2] presented a validated steady-state ORC model and an optimization methodology for solar ORCs based on finite-time analysis but no simulation of the entire solar ORC system.

Other authors have focused on ORC or thermal storage dynamics in isolation. Wei *et al.* [3] developed a dynamic ORC model and examined the efficiency of moving boundary versus discretized heat exchanger techniques when compared to experimental data. Casella *et al.* [4] developed a dynamic ORC model for normal operation by building on the existing ThermoPower library in the Modelica modeling language. This model was validated in steady-state and transient conditions based on a grid-connected turbogenerator with natural gas or diesel generator exhaust as the heat source. It was also used to simulate feedback control to match desired turbine inlet temperature by varying pump speed. McMahan [2] examined the accuracy and computational efficiency of several techniques for simulating packed-bed storage dynamics in charging/discharging and idle conditions.

In addition, Twomey *et al.* [5] simulated grid-connected solar ORC system dynamics with the solar loop modeled as a single lumped component and solar irradiance represented by a daily half sine curve whose amplitude was adjusted for monthly averages to estimate daily and annual power generation.

In this work, a model for the dynamics of the solar ORC system is developed to evaluate the impact of highly transient heat sources and sinks, thermal storage, and the variable loads associated with distributed generation. Over the past several years, researchers at MIT and University of Liège have collaborated with the non-governmental organization STG International to design a micro-CSP plant suitable for rural power generation. The design of this system has been described extensively in [6]. Several field prototypes for the proposed system have been installed. In addition, a pilot system, pictured in Fig. 1, resides at Eckerd College in St. Petersburg, Florida, and this system is used as the basis for the dynamic model. Table 1 lists the components of the system and the major modeling parameters. Figure 2 presents a flow diagram identifying the relationships between the major components. The target net output power of the system is 3 kWe at an overall efficiency from solar power input to ORC power output of 3% and ORC thermal efficiency from evaporator heat input to net power output of 8%.

To study possible control schemes for the proposed system, a dynamic model has been developed in the Modelica modeling language using the ThermoCycle library. The dynamic model is based on detailed steady-state component models, which are implemented in EES and validated to data where available. The dynamic model in its current form is used to make qualitative assessments of several control decisions based on realistic solar irradiance input representing four reference days. Future analysis will survey a wider range of environmental conditions to make quantitative determinations on the efficacy of each control decision. The simulations include an approximation for startup and shutdown, which avoids the numerical issues associated with the discontinuities in the working fluid density derivative present during such rapid phase changes.

STEADY-STATE MODELING

The steady-state models have been matched to data where available, and they are used to provide initial values, heat transfer coefficients, and pressure drops for the dynamic simulation and for its validation when run to steady-state. In addition, the steady-state system model is used to perform an optimization analysis for input to a real-time control strategy discussed in the section on dynamic modeling.

Evaporator/Recuperator

The brazed plate heat exchangers are modeled using the log mean temperature difference method, where the recuperator con-

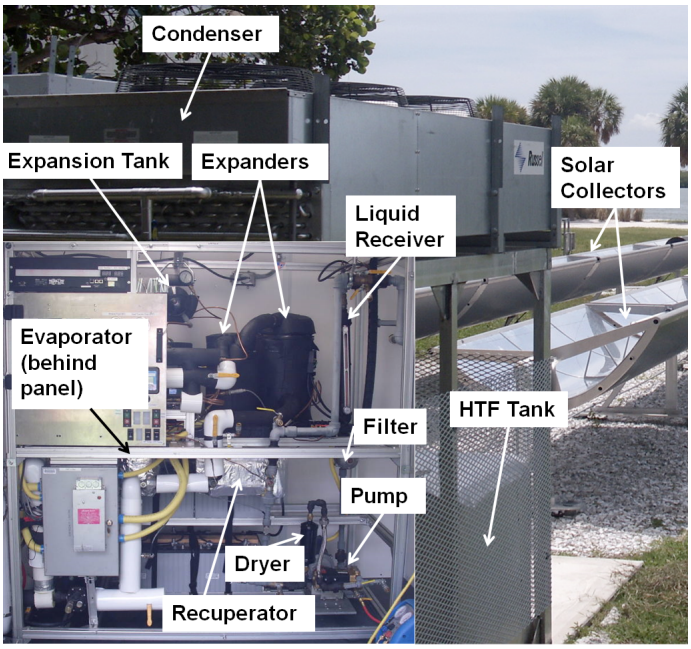

FIGURE 1. PILOT SOLAR ORC SYSTEM SHOWING THE AIR-COOLED CONDENSER, THERMAL STORAGE, AND SOLAR COLLECTORS WITH THE ORC IN THE LOWER LEFT INSET.

sists of single-phase liquid or vapor regions and the evaporator includes liquid, two-phase, and vapor regions. Heat transfer coefficients and frictional pressure drops are determined using Thonon for single-phase flow [7] and Hsieh and Lin for two-phase flow [8]. To speed the iteration process for the full system model, the pressure drops, while calculated, are not implemented. With pressure drops typically below 10 kPa for these heat exchangers, the impact of internal pressure variation on heat transfer should be negligible.

Expander-generators

There are two hermetic scroll compressors modified to run as expander-generators. Neglecting ambient heat losses, the expanders are characterized by their filling factor and isentropic efficiency. Filling factor, ϕ, is defined as the ratio of real to ideal mass flow rate or

$$\phi = \frac{\dot{m} \cdot v_{su}}{\dot{V}_s} = \frac{\dot{m} \cdot v_{su}}{V_s \cdot N_{rot}}. \quad (1)$$

Isentropic efficiency, η_s, is the ratio of real to ideal power generated or

$$\eta_{s,exp} = \frac{\dot{W}_{el}}{\dot{m} \cdot (h_{su} - h_{ex,s})}. \quad (2)$$

The electrical power is used here as the asynchronous generator is integrated with the expander in a hermetic shell. The internal irreversibilities accounted for in the isentropic efficiency are thus a combination of both the fluidic and electrical losses.

The expander model is based on Lemort *et al.* [9] who created a detailed model accounting for multiple types of losses and validated to prototype test data. To extend this model to expanders of various swept volumes, the validated model was exercised over 800 different working conditions that bracket the operating envelope of the experimental system, and polynomial fits were generated to correlate ϕ and $\eta_{s,exp}$ as a function of supply pressure and pressure ratio. It is assumed that the filling factor and isentropic efficiency remain comparable for the same supply pressure and pressure ratio regardless of swept volume.

Condenser

Because of its complex geometry, illustrated for one tube bank in Fig. 3, the finned-tube condenser is more difficult to split into zones as in the evaporator model. Therefore, a discretized model is developed. The condenser is approximated as a set of 12 identical parallel tube banks each consisting of 12 tubes in 5 rows. Each tube is discretized into n elements for a total of 12 x n refrigerant elements per tube bank. As the banks are assumed identical, the set of equations for a single bank is sufficient to model the entire exchanger.

The air flowing over the tube bank is assumed to be well-mixed between tube rows as this is conservative and analysis showed a negligible difference in results assuming mixed or unmixed air [10]. Therefore, the supply air temperature for each row is assumed to be the average of the exhaust temperatures for the cells below. Tube-tube heat transfer due to conduction through the fins is neglected when, in fact, the distance between the tubes suggests they would transfer some heat with each other representing a potential refinement for future models [10]. An energy balance is performed for each tube cell with the air treated as a constant specific heat fluid, while the refrigerant specific heat is allowed to vary.

The refrigerant-side heat transfer coefficient is determined using Gnielinski (Re<100,000) or Dittus-Boelter (Re>100,000) for single-phase flow [11] and Shah for two-phase flow [12]. The air-side heat transfer coefficient and pressure drop are determined using Kim *et al.* [13]. The fin efficiency is calculated, neglecting the corrugation, using the Schmidt method [14] for approximating the hexagonal fins as circular fins of equivalent height. The model also neglects the contribution of water in the air to heat transfer, another possible refinement. As in the evaporator/recup-

TABLE 1. PILOT SYSTEM COMPONENTS AND MAJOR MODELING PARAMETERS.

Component	Description	Supplier	Parameter	Value
Heat transfer fluid	Propylene glycol	Various		
Collectors	Single-axis SopoNova parabolic trough, SOLEC HI/SORB II selective coating, air-filled annulus between absorber and glazing	Sopogy	A_s	104 m^2
			L_{col}	73 m
			W_{col}	1.4 m
			D_o	25 mm
Storage tank	Double-wall plus insulation, 3696K71	McMaster	V	0.79 m^3
			t_{ins}	25 mm
			k_{ins}	3.9e-2 $W(mK)^{-1}$
HTF pump	Gear, NG11V-PH	Dayton	V_s	24e-6 m^3
HTF motor	48VDC permanent magnet	Leeson	$\dot{W}_{nom}$	373 W
Working fluid	HFC-245fa	Honeywell		
Evaporator	Brazed Plate, BP415-050	ITT Brazepak	A_s	2.4 m^2
			V	2.5e-3 m^3
			M_w	11 kg
Recuperator	Brazed Plate, BP410-030	ITT Brazepak	A_s	0.73 m^2
			V	8.4e-4 m^3
			M_w	3.7 kg
Condenser	Air-cooled finned-tube with hexagonal tube array, Multicon CAC-28-G	Russell	$A_{tubeside}$	13 m^2
			$A_{finside}$	360 m^2
			$V_{tubeside}$	4.0e-2 m^3
Liquid receiver	Length of pipe plus sight glass	Various	V	1.3e-3 m^3
Expander-generators	Hermetic scroll induction machine, ZR48	Copeland	V_s	22e-6 m^3
	ZR125		V_s	56e-6 m^3
WF pump	Plunger, PowerLine Plus 2351B-P	Hypro	V_s	8.7e-6 m^3
WF motor	48VDC permanent magnet	Leeson	$\dot{W}_{nom}$	746 W

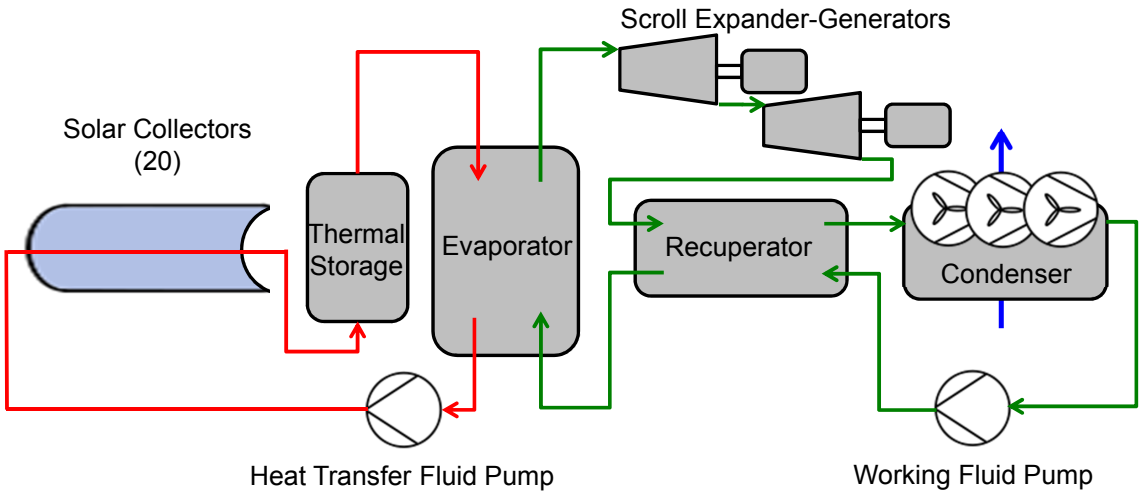

FIGURE 2. FLOW DIAGRAM FOR THE MICRO-CSP PLANT WITH PROPYLENE GLYCOL AS HEAT TRANSFER FLUID (SHOWN IN RED) AND HFC-245FA AS WORKING FLUID (SHOWN IN GREEN). CONDENSER COOLING AIR IS SHOWN IN BLUE.

erator models, to speed the iteration process, while refrigerant pressure drop is calculated from Petukhov [11] for single-phase flow and Choi *et al.* [15] for two-phase flow, it is not implemented in the heat transfer model. For condensing temperatures below 15°C, for which pressure drop can exceed 30 kPa and therefore no longer has a negligible impact on heat transfer, a more complete model may be necessary.

For computational efficiency, the detailed heat transfer model is represented in this study by a linear function with heat transfer correlated to refrigerant supply temperature, air supply temperature, and air mass flow rate and an assumed temperature defect of 10°C between working fluid exhaust and ambient air temperatures (as in the optimization analysis described in the Control Unit section) [10]. An expanded analysis developing a non-linear correlation for a range of temperature defects and working conditions is presented in [10], which may be utilized in a more computationally-intensive approach optimizing plant net power as a function of fan effort.

The condenser fan power consumption is correlated to experimental data using a logarithmic fit as a function of the volume flow rate of the air with R^2 = 86.74% [10].

Pumps/Motors

A pump's global isentropic efficiency, η_p, including both electromechanical and internal losses, is defined by:

$$\eta_p = \eta_{em,p} \cdot \eta_{s,p} = \frac{\dot{W}_s}{\dot{W}_{el}} = \frac{\dot{m} \cdot (h_{ex,s} - h_{su})}{\dot{W}_{el}} \approx \frac{\dot{m} \cdot v_{su} \cdot (p_{ex} - p_{su})}{\dot{W}_{el}}. \quad (3)$$

For the working fluid (WF) pump, the isentropic efficiency is derived from manufacturer data and then correlated using a second-order polynomial fit as a function of normalized outlet pressure with R^2 = 98.75% [10]. Volumetric efficiency is neglected in the manufacturer data. The motor efficiency is also derived from manufacturer data and correlated using a sixth-order polynomial fit as a function of fraction of rated mechanical power with R^2 = 99.83% [10].

For the heat transfer fluid (HTF) pump, the measured electrical power output from experimental data is correlated to the measured volume flow rate and supply temperature using a second-order polynomial fit with R^2 = 99.55% [10]. Although the HTF pump is also separated from the motor, there was not enough information in the available data to distinguish the electromechanical losses from the internal irreversibilities. This approximation would result in an error in outlet enthalpy, but since enthalpy change in a pump is small compared to the other components, the effect should be negligible.

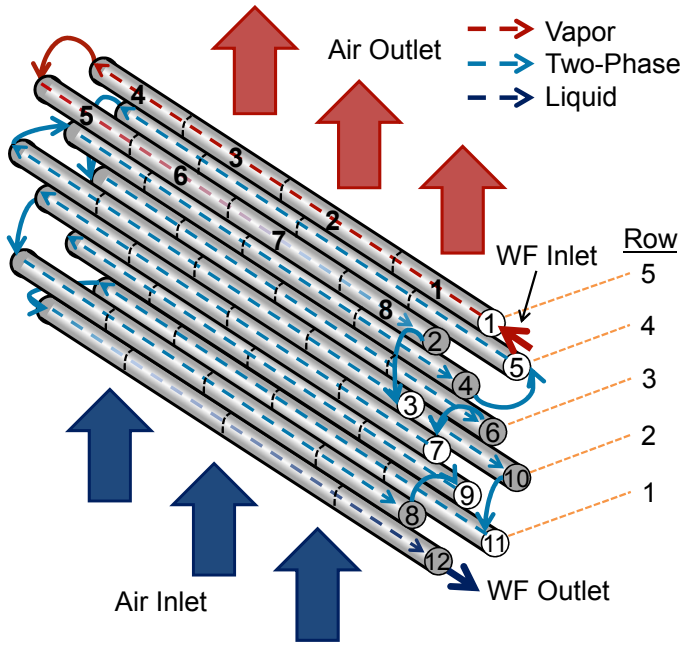

FIGURE 3. MODELING SCHEMATIC OF CONDENSER TUBE BANK. REFRIGERANT ENTERS AS A VAPOR ON THE TOP RIGHT AND TRAVELS BACK AND FORTH FROM TUBE 1 TO TUBE 12 ON THE BOTTOM LEFT WHILE CONDENSING. DASHED BLACK LINES AND BOLD NUMBERS (FOR THE FIRST TWO TUBES) NOTIONALLY REPRESENT THE DISCRETIZATION OF FLUID CELLS IN THE TUBES AND THE HEXAGONAL PRISM OF AIR AND FINS (NOT SHOWN) SURROUNDING THE TUBE SECTION. DASHED ORANGE LINES REPRESENT THE PLANES OF EACH TUBE ROW.

There is currently no cavitation model for the pumps, a possible future improvement.

Solar Collectors

The solar array is composed of 20 parabolic trough collectors. The collectors are modeled using the one-dimensional energy balance around the discretized heat collection element of Forristall [16]. Knowing the collector geometry, solar irradiance, ambient temperature, wind speed, incidence angle, mass flow rate, and inlet temperature to the collector, the fluid outlet temperature can be calculated. Forristall's model, available in EES, is parameterized for the collector geometry of the pilot system and validated using the manufacturer specifications adjusted according to experimental data from commissioning the solar field [10].

To reduce simulation time in the dynamic model, the validated model is exercised over 400 working conditions to determine the fitting parameters for the correlation developed by [17]

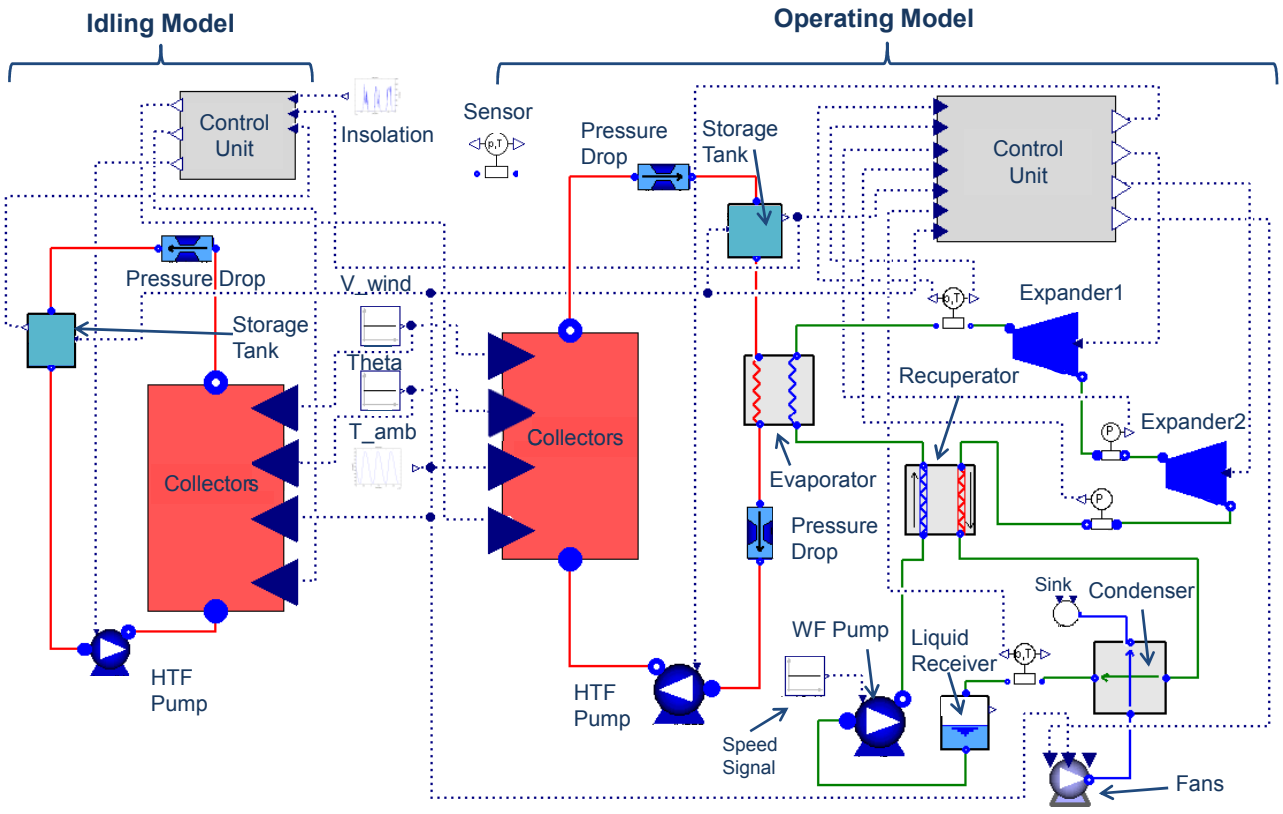

FIGURE 4. MODELICA INTERFACE FOR THE DYNAMIC SYSTEM MODEL WITH THE HTF REPRESENTED BY RED LINES, REFRIGERANT BY GREEN LINES, AND COOLING AIR BY BLUE LINES. SENSED PARAMETERS AND CONTROL SIGNALS ARE REPRESENTED BY DOTTED LINES.

for heat loss in Wm^{-1} as a function of HTF and ambient temperatures, irradiance, incidence angle modifier, and wind speed:

$$\begin{aligned} HL =& c_0 + c_1 \cdot (T_{HTF} - T_{amb}) + c_2 \cdot T_{HTF}^2 \\ &+ c_3 \cdot T_{HTF}^3 + c_4 \cdot I_b IAM cos\theta \cdot T_{HTF}^2 \\ &+ \sqrt{v_w} \cdot (c_5 + c_6 \cdot (T_{HTF} - T_{amb})) \end{aligned} \quad (4)$$

with $R^2 = 99.85\%$ where the coefficients, c_k, are provided in [10]. This heat loss term participates in a simplified energy balance between the fluid and the solar input equating the heat convected to the fluid with the solar input reduced by the correlated heat loss.

DYNAMIC MODELING

Modelica is an acausal object-oriented programming language facilitating the deconstruction of a complicated system into its simpler component parts. In such a language, differential-algebraic equations can be written directly for each part without regard for order, and the models can be connected via ports, typically relating mass flow, pressure, and enthalpy between components. The models for the solar ORC plant either come directly from the open-source ThermoCycle library [18] or build upon the available components, and the fluid properties are determined using the open-source CoolProp library [19]. The Tabular Taylor Series Expansion method is used to improve computational efficiency in calculating fluid properties. Figure 4 illustrates the plant schematic in the Dymola Modelica interface.

The model aims to capture the important dynamics of the system. With much shorter time constants compared to the other components, the dynamic response of the expanders and pumps is neglected. Therefore, these dynamic component models are equivalent to their steady-state representation.

Evaporator/Recuperator

The evaporator and recuperator are modeled as discretized finite volume counterflow heat exchangers. Figure 5 demonstrates that the heat exchangers are divided into three compo-

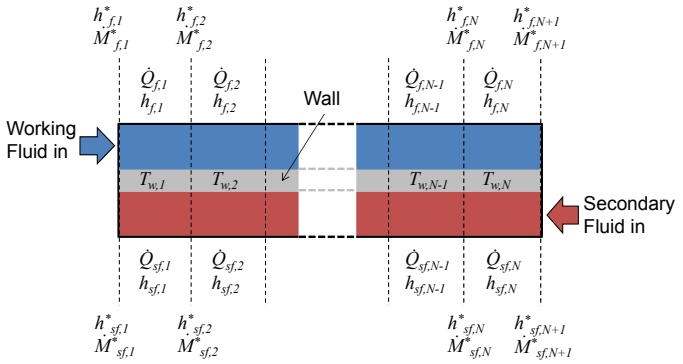

FIGURE 5. DISCRETIZED HEAT EXCHANGER MODEL SHOWING CELL VS NODE PARAMETERS. THE NODE PARAMETERS ARE INDICATED WITH A *. FIGURE IS BASED ON [20].

nents: working fluid, secondary fluid, and metal wall as if the multiple plates in a brazed plate exchanger were one long plate. The WF and secondary fluid sides are based on dynamic mass and energy balances, while the momentum balance is considered static. For a detailed description of the models, see [20].

Condenser

The refrigerant and metal wall cell dynamic equations are identical to those of the evaporator and recuperator, but the overall discretization scheme is slightly different due to the cross-flow of the air as shown in Fig. 6. The air cells are assumed to have negligible dynamics.

The next building block in the dynamic model is a row of tubes. Each row consists of n tubes per row x m cells per tube such that there are n x m refrigerant, metal wall, and air cells plus corresponding pressure drop components for the air cells. Also required are splitter and joiner components to divide the incoming air from the preceding row among the refrigerant cells and rejoin the air cells after they have transferred heat with the metal/refrigerant.

Finally, the five rows of two or three tubes are linked to complete the condenser model. The condenser fan power demand is identical to that of the steady-state model.

Liquid Receiver

The liquid receiver is assumed to be in thermodynamic equilibrium at all times: the vapor and liquid are saturated at the given pressure. It is modeled by the same energy and mass conservation laws as in the discretized heat exchangers, but the exit condition is imposed to be a saturated liquid. Since the control unit regulates condensing pressure, the pressure in the liquid receiver is set by the saturation pressure in the condenser. Initialization sets either the initial pressure or liquid level.

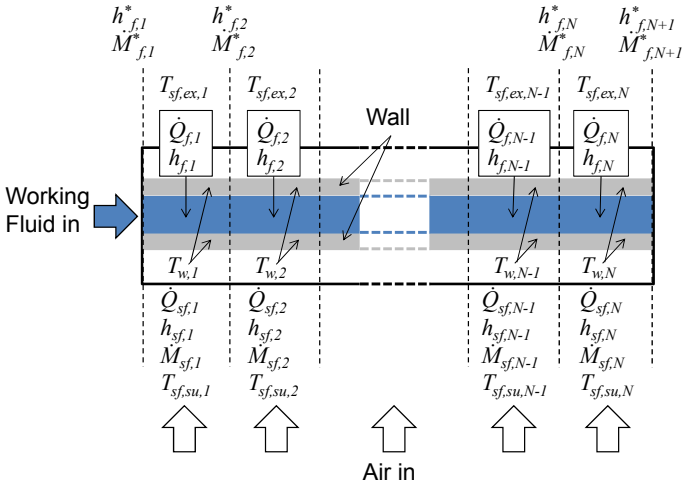

FIGURE 6. SIDE VIEW FOR A SINGLE TUBE OF THE DISCRETIZED CONDENSER MODEL SHOWING CELL VS NODE PARAMETERS. THE NODE PARAMETERS ARE INDICATED WITH A *.

Solar Collectors

The solar collector model consists of two models connected by a thermal port: one representing the fluid dynamics in the discretized absorber tube and the other representing the collector thermal and optical efficiency based on the fluid temperature and environmental conditions. As discussed previously, the efficiency, or heat loss, model is determined using a regression of the detailed Forristall model fit to the manufacturer specification and adjusted to experimental data, where the environmental inputs are solar irradiance, ambient temperature, wind velocity, and incidence angle. The discretized fluid cells in the absorber tube are modeled in the same way as the secondary fluid in the evaporator.

For computational efficiency, rather than being calculated in each cell, the pressure losses are combined into lumped models after the heat exchanger and collectors as shown in Fig. 4. A relation for pressure drop in off-design conditions is determined by assuming a constant friction factor:

$$\frac{\Delta p}{\nu \cdot \dot{m}^2} = \frac{2 \cdot f \cdot L_{col} \cdot A_{cross}^2}{D_h} = constant \rightarrow$$

$$\Delta p = \Delta p_{nom} \cdot \frac{\nu}{\nu_{nom}} \cdot \left(\frac{\dot{m}}{\dot{m}_{nom}} \right)^2 \quad (5)$$

The nominal conditions are defined using the steady-state model results for a representative working condition.

Storage Tank

Pressure is imposed in the storage tank, which is modeled as a well-mixed (single element) control volume accounting for thermal energy losses due to conduction and convection through the top, sides, and bottom walls and insulation.

Control Unit

Two control strategies have been evaluated. The first, referred to as $P_{ev,opt}$, aims to track the optimum evaporation pressure within physical constraints, e.g., expander speeds, identified by exercising the steady-state model over 30 working conditions. A second-order polynomial was fit to these results to define the optimum evaporation pressure as a function of the HTF supply temperature and ambient temperature with R^2 = 99.26% [10]. The second control strategy, referred to as $T_{ev,const}$, aims to maintain a constant evaporation temperature.

In addition, in both strategies, the superheat and condenser temperature defect between WF exhaust and air supply are controlled to a constant 5°C and 10°C, respectively. Because each expander's isentropic efficiency is modeled using a polynomial as a function of supply pressure and pressure ratio, it is possible to find an analytical solution for the optimum intermediate pressure by maximizing the equation for the combined efficiency given the inlet and outlet pressures [20]. For both strategies, the WF pump speed is held constant, although further optimization may be possible by relaxing this constraint. This topic will be addressed in future work.

During normal operation, the control unit regulates system components to achieve the set points by utilizing four PI controllers illustrated in Fig. 7 for the $P_{ev,opt}$ strategy. PI control is selected because of its reduced sensitivity to measurement noise compared to PID control. The sensor dynamics are currently neglected. The speed of the HTF pump is used to regulate superheat; the speed of Expander 1 is used to regulate either $P_{ev,opt}$ or $T_{ev,const}$; the speed of Expander 2 is used to regulate optimum intermediate expander pressure; and the mass flow rate of the condenser fans (as a simplified proxy for fan speed and number of operating fans) is used to control the condensing pressure. For the $T_{ev,const}$ strategy, the P_{ev} block in Fig. 7 would be replaced with a constant set point and the process variable for saturation temperature would be determined using the ΔT_{ev} block.

The controllers are tuned manually with the other controllers disabled by varying the proportional gain and integral time after a step is introduced. It is assumed that the closed-loop system is decoupled and behaves linearly and that the same tuning parameters can be used for the two strategies. A more robust control tuning and design is proposed in the Future Work section.

Startup/Shutdown.

To simulate the daily power cycle, the control must have the ability to shut down the ORC at the end of the day or at any time when there is insufficient irradiance to warrant running the pumps. Similarly, it will need to simulate startup. Numerical simulation of startup or shutdown is difficult due to flow reversals, chattering around zero flow, and unphysical flow rate generation due to a discontinuity in the WF density derivative [21]. To approximate these conditions while avoiding numerical issues, duplicate models representing operating and idling modes (see Fig. 4) are simulated concurrently, transferring state variables to achieve an energy balance between the two when startup and shutdown, which are modeled as instantaneous events, are triggered. As experimental data indicates that the time scale of startup or shutdown is on the order of minutes, the impact of this approximation on a full-day simulation is expected to be negligible. However, ORC thermal inertia during these events is also neglected, so future analysis is planned to integrate this effect.

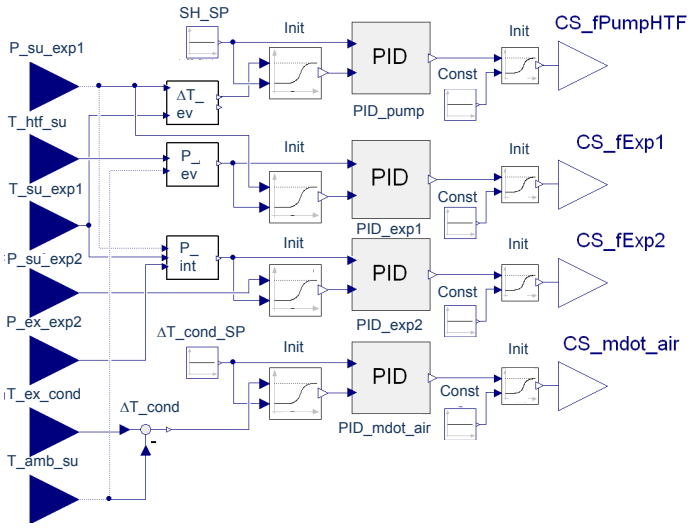

FIGURE 7. MODELICA INTERFACE FOR THE $P_{ev,opt}$ STRATEGY CONTROL UNIT. UPPER LEFT ARROWS OF PID REPRESENT SET POINTS, LOWER LEFT REPRESENT PROCESS VARIABLES, AND RIGHT REPRESENT CONTROL SIGNALS.

RESULTS

The two control strategies are compared by simulating the system response to a solar irradiance dataset comprising four reference days that bracket a wide range of irradiance conditions from clear sky to severe overcast. For this preliminary assessment, T_{amb}, approximated as a sine curve, is the same for each of the four days and θ and v_{wind} are set to zero. At the beginning of the first day, the storage tank is initialized to 135°C, 10°C below the chosen shutdown trigger temperature of 145°C (approximately the overnight temperature loss). This shutdown trigger temperature is chosen to maintain the 5°C of superheat given the

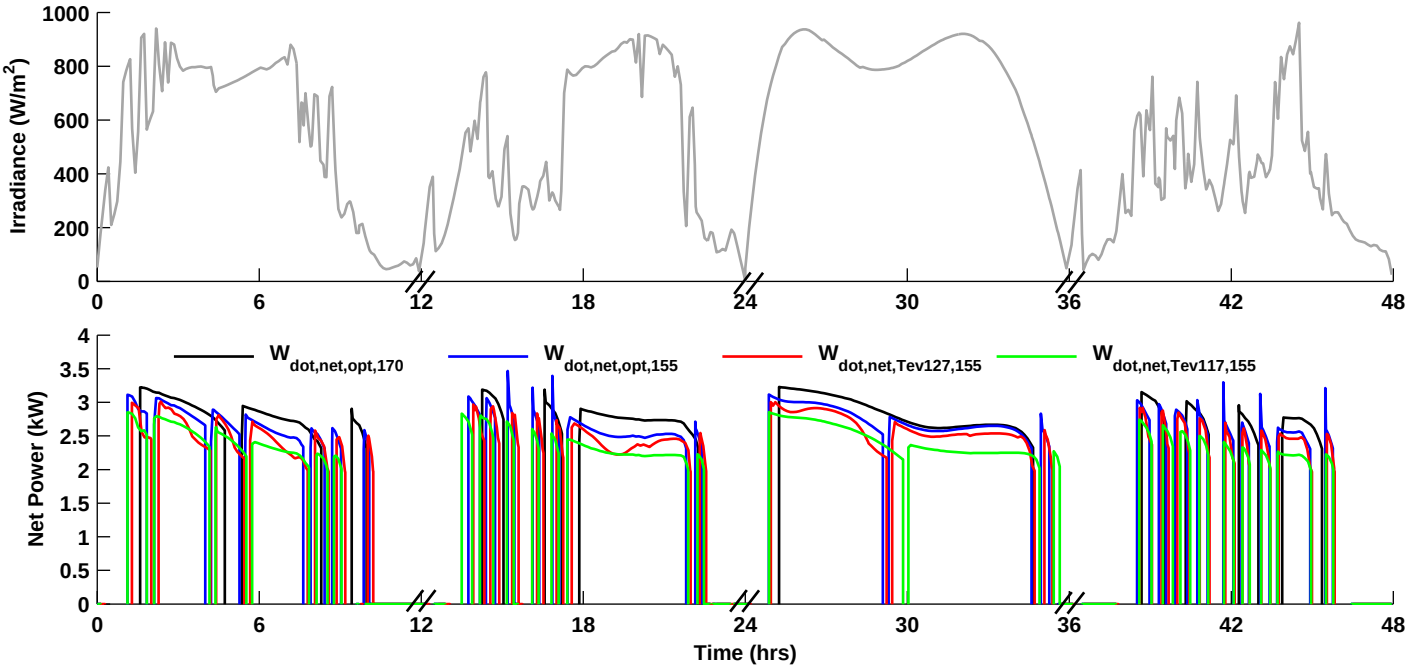

FIGURE 8. DIRECT NORMAL IRRADIANCE AND POWER GENERATED VIA CONTROL STRATEGIES $P_{ev,opt}$ AND $T_{ev,const}$. THE FINAL NUMBERS IN THE LEGEND INDICATE THE STARTUP TRIGGER TEMPERATURE. THE DIAGONAL HATCH MARKS ON THE X-AXES INDICATE THAT THE OVERNIGHT RESULTS, FOR WHICH THE PLANT IS SHUT DOWN, ARE NOT SHOWN.

hardware limit of 1800 rpm imposed for the HTF pump. The startup trigger is set to 155°C. The $T_{ev,const}$ strategy is analyzed with two different evaporating temperatures, 117°C and 127°C, now referred to as $T_{ev,117}$ and $T_{ev,127}$, respectively. A T_{ev} of 127°C is the highest at which the 5°C of superheat can be maintained within the HTF pump hardware limit under these conditions.

Figure 8 shows the net power generated for each strategy in addition to the assumed irradiance profile. The vertical drops indicate that the tank reached 145°C and a shutdown was executed. For these four reference days, the $T_{ev,const}$ strategy at T_{ev} = 117°C, the $T_{ev,const}$ strategy at T_{ev} = 127°C, and the $P_{ev,opt}$ strategy generate 62.7 kWh, 65.5 kWh, and 70.0 kWh of energy, respectively. In other words, as a result of its ability to flexibly adapt to varying ambient conditions, the $P_{ev,opt}$ strategy generates 12% and 7% more energy than the $T_{ev,117}$ and $T_{ev,127}$ strategies, respectively. It must be noted, however, that these results do not take into account the potential effects of repeated ORC startup/shutdown cycling (e.g., due to the heat capacity of the hardware or the need for load following, which were neglected in this model); a follow-on study to investigate the trade-offs between increasing thermal storage size (and ambient losses) and decreasing operational cycling is suggested.

Having validated that an optimized pressure strategy is more effective, the role of startup trigger temperature on cycling is further investigated. At a trigger of 170°C, the initial system startup in the morning is delayed, but fewer shutdowns occur during the day once ORC operation begins. Energy generated also increases slightly by 0.1% versus the 155°C startup temperature. Fewer startup and shutdown cycles implies improved maintenance profiles and extended mean time between failure of components.

CONCLUSIONS

A model capturing the important dynamics of a micro-CSP system with thermal storage capable of responding and adapting to rapid environmental variations has been developed. The dynamic model is based on detailed steady-state models validated to data where available. A strategy for approximating startup and shutdown while avoiding the numerical issues associated with rapid phase changes has been proposed to facilitate multiple-day simulations. To the authors' knowledge, this is the first model capable of continuously simulating through startup and shutdown in addition to coupling a dynamic thermodynamic model of the power cycle with dynamic models of the collectors and tank.

In this preliminary assessment based on a solar irradiance dataset spanning four reference days, the $P_{ev,opt}$ strategy that adjusts the operating point based on the boundary conditions generates 7% more energy than the $T_{ev,const}$ strategy evaporating at 127°C. Moreover, startup trigger temperature plays an important role in system dynamics and performance, with advantages in se-

lecting for an operational envelope at higher temperatures of the working fluid. In this study, increasing the startup trigger temperature from 155°C to 170°C recovers 0.1% more energy with fewer shutdowns during the day, which should reduce maintenance costs.

FUTURE WORK

Further investigation of seasonal timescale environmental influences and examination of alternative trigger temperatures and storage tank sizes is warranted. In addition, the full system model should be validated to the pilot system in steady-state. The correlations used for the expander properties were developed for grid-synchronized, constant-speed expanders, and these should be validated for variable-load and asynchronous operation.

A more realistic representation of sensor dynamics would help indicate whether the proposed control schemes are viable as parameterized. A more rigorous control design process should lead to a more responsive, robust control system. The typical process would include the following steps: modeling, linearizing, designing the controllers, and verifying by closed-loop comparison between the linear and nonlinear models.

In the present work, the ORC thermal inertia is neglected during startup and shutdown transients. In the future, a model that accounts for this effect would allow for a more accurate comparison of the different control strategies.

REFERENCES

[1] Orosz, M., 2012. "Thermosolar and photovoltaic hybridization for small scale distributed generation: applications for powering rural health". PhD Thesis, MIT, Cambridge, MA, Jun.

[2] McMahan, A., 2006. "Design and optimization of organic Rankine cycle solar-thermal powerplants". MS Thesis, University of Wisconsin-Madison, Aug.

[3] Wei, D., Lu, X., Lu, Z., and Gu, J., 2008. "Dynamic modeling and simulation of an Organic Rankine Cycle (ORC) system for waste heat recovery". *Applied Thermal Engineering,* ***28***, pp. 1216–1224.

[4] Casella, F., Mathijssen, T., Colonna, P., and van Buijtenen, J., 2013. "Dynamic Modeling of Organic Rankine Cycle Power Systems". *J. of Eng. Gas Turbines and Power,* ***135***, Apr., pp. 042310–1–12.

[5] Twomey, B., Jacobs, P., and Gurgenci, H., 2013. "Dynamic performance estimation of small-scale solar cogeneration with an organic Rankine cycle using a scroll expander". *Applied Thermal Engineering,* ***51***, pp. 1307–1316.

[6] Quoilin, S., Orosz, M., Hemond, H., and Lemort, V., 2011. "Performance and design optimization of a low-cost solar organic Rankine cycle for remote power generation". *Solar Energy,* ***85***, pp. 955–966.

[7] Thonon, B., 1995. "Recent research and developments in plate heat exchangers". *Fuel and Energy Abstracts,* ***36***.

[8] Hsieh, Y., and Lin, T., 2002. "Saturated flow boiling heat transfer and pressure drop of refrigerant R-410a in a vertical plate heat exchanger". *Int. J. Heat Mass Transfer,* ***45***(5), pp. 1033–1044.

[9] Lemort, V., Declaye, S., and Quoilin, S., 2012. "Experimental characterization of a hermetic scroll expander for use in a micro-scale Rankine cycle". In Part A: J. Power and Energy, Vol. 226 of *Proc. IMechE*, pp. 126–136.

[10] Ireland, M., 2014. "Dynamic Modeling and Control Strategies for a Micro-CSP Plant with Thermal Storage Powered by the Organic Rankine Cycle". MS Thesis, MIT, Cambridge, MA, Feb.

[11] Incropera, F., and DeWitt, D., 2007. *Fundamentals of Heat and Mass Transfer*. Wiley, New York.

[12] Shah, M., 1979. "A general correlation for heat transfer during film condensation in pipes". *Int. J. Heat Mass Transfer,* ***22***, pp. 547–556.

[13] Kim, N., Youn, B., and Webb, R., 1999. "Air-side heat transfer and friction correlations for plain fin-and-tube heat exchangers with staggered tube arrangements". *Trans. ASME,* ***121***, Aug., pp. 662–667.

[14] Schmidt, T., 1949. "Heat transfer calculations for extended surfaces". *J. ASHRAE*, Apr., pp. 351–357.

[15] Choi, J., Kedzierski, M., and Domanski, P., 1999. A Generalized Pressure Drop Correlation for Evaporation and Condensation of Alternative Refrigerants in Smooth and Microfin Tubes. Technical Report NISTIR 6333, NIST, Gaithersburg, MD, Oct.

[16] Forristall, R., 2003. Heat Transfer Analysis and Modeling of a Parabolic Trough Solar Receiver Implemented in Engineering Equation Solver. Technical report, NREL, Golden, CO, Oct.

[17] Burkholder, F., and Kutscher, C., 2009. Heat Loss Testing of Schott's 2008 PTR70 Parabolic Trough Receiver. Technical report, NREL, Golden, CO, May.

[18] Quoilin, S., Desideri, A., Wronski, J., Bell, I., and Lemort, V., 2014. "ThermoCycle: A Modelica library for the simulation of thermodynamic systems". In 10th International Modelica Conference.

[19] Bell, I., Wronski, J., Quoilin, S., and Lemort, V., 2014. "Pure- and Pseudo-Pure Fluid Thermophysical Property Evaluation and the Open-Source Thermophysical Property Library CoolProp". *Ind. Eng. Chemistry Research*.

[20] Quoilin, S., 2011. "Sustainable Energy Conversion Through the Use of Organic Rankine Cycles for Waste Heat Recovery and Solar Applications". PhD Thesis, University of Liège, Liège, Belgium, Oct.

[21] Quoilin, S., Bell, I., Desideri, A., and Lemort, V., 2014. "Methods to increase the robustness of finite-volume flow models in thermodynamic systems". *Energies*.